Compact, eye-safe polarization light detection and ranging system at 1550 nm wavelength for aerosol anomaly detection

SEBASTIAN ZAJONZ*, OLIVER KLIEBISCH, FRANK DUSCHEK, ARNE WALTER AND THOMAS DEKORSY

German Aerospace Center, Institute of Technical Physics, Pfaffenwaldring 38-40, 70569 Stuttgart, Germany
sebastian.zajonz@dlr.de

Abstract:

The study of atmospheric aerosols, which are defined as fine particles suspended in the atmosphere, using light detection and ranging (lidar) techniques is well-established. This work presents the real-time measurement of aerosol anomalies (i.e., concentration hotspots) using an eye-safe, portable polarization lidar system operating at a wavelength of 1550 nm. The system, mainly consisting of commercial off-the-shelf components, has a spatial resolution of about 3 m and a weight of less than 10 kg. As a proof of concept, this paper discusses the classification of aerosols and their physical characteristics, as well as the implications of their presence in the atmosphere. Therefore, the aerosols water mist, sand, and Arizona road dust were measured in a distance of 100 m.

1. Introduction

Aerosols affect numerous environmental and health-related processes. Their properties and behavior significantly influence global climate regulation, air quality, human health, and visibility [1, 2]. Aerosols are classified based on size and chemical composition. The United Nations and World Health Organization use two major categories: PM2.5 (particles with aerodynamic diameters $\leq$ 2.5 µm) and PM10 ($\leq$ 10 µm) [3]. Particle size determines atmospheric lifetime and health effects; smaller particles like PM2.5 remain airborne longer and can penetrate deeper into the respiratory tract [4]. Aerosol behavior also depends on their chemical nature and environmental conditions such as humidity and temperature [5]. These variables influence physical properties like shape and density, which in turn affect transport and reactivity. The shape of aerosols varies according to their origin and phase. Liquid aerosols are often spherical due to surface tension, while solid aerosols exhibit irregular geometries. Bioaerosols, including fungal spores and bacteria, display diverse morphologies, ranging from spherical to rod-shaped forms [6]. Shape serves as a classifier and influences interactions with light. Light scattering by aerosols are governed by their size, refractive index, and shape. Polarization effects are particularly significant for remote sensing applications and are used to extract information about particle characteristics [7]. Health impacts of aerosols depend on particle nature and atmospheric concentration. Fine particles, especially PM2.5, are linked to cardiovascular and respiratory illnesses [2]. Medium risk is associated with concentrations between 10 and 25 $\mu g/m^3$, roughly equating to 10,000 particles per milliliter of air [8]. Aerosols originate from both natural and human-made sources. Industrial activities, fire incidents, fermentation in bioreactors, and agricultural spraying [9] are significant contributors. Under certain operating conditions, these sources may produce high aerosol concentrations, posing serious environmental and health risks [8]. Due to the variability and risks associated with aerosol emissions, monitoring systems are essential. In this work, we propose a remote sensing-based method that uses polarization-sensitive light scattering to quantify aerosol quantity and derive morphological properties. For this purpose, a polarization lidar was developed that operates in the eye-safe wavelength range of 1550 nm with kHz repetition rates and high spatial resolution below 3 m.

2. System design

In contrast to other polarization lidars optimized for atmospheric research, where eye safety and portability are secondary considerations, for example [10] [11], the polarization lidar, which is presented as follows, prioritizes an eye-safe wavelength, a portable system, and high spatial resolution.

A bistatic non-coaxial design is chosen for the following reasons. First, this design allows to achieve good near-field or good far-field sensitivity by adjusting the inclination between transmitter and receiver and avoids the central obstruction which limits the near-field sensitivity [12]. Second, a polarization lidar requires splitting the received light into its base polarization states, which is not easily achieved for a monostatic system where the polarization property of light is already used to separate the transmitted beam from the received beam. The optical components of the bistatic non-coaxial system can be divided into two distinct paths: the transmitter path and the receiver path. The arrangement of the components is illustrated in Fig. 1.

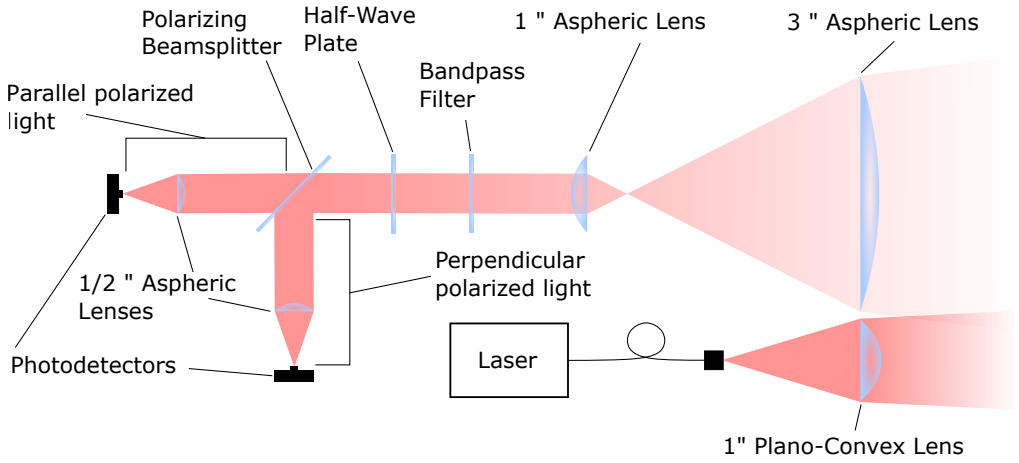

Fig. 1. Arrangement of the main components of the polarization lidar and the light passing through the system.

The transmitting path of the lidar system comprises a pulsed fiber laser and a 1" plano-convex lens with a focal length of 150 mm. The laser utilized in the polarization lidar is a Lumibird PK50D 1550 nm laser, with a pulse length of 8 ns and an average power of 1 W.

In order to receive the backscattered light, a 3" aspheric lens with a focal length of 150 mm is used. The 3" aperture was chosen as a compromise between sensitivity and system size. To produce a collimated beam in the receiving path, a 1" aspheric lens with a focal length of 20 mm is positioned in a Kepler telescope arrangement with the 3" aspheric lens. Subsequently, the bandpass filter, the half-wave plate, and the polarizing beamsplitter are positioned within the collimated beam, following the placement of the 1" aspheric lens. The bandpass filter serves to absorb wavelengths that are not desired, while the half-wave plate is used for the purpose of correcting crosstalk. The polarizing beamsplitter divides the incoming beam into two distinct polarization states: parallel, which traverses the beamsplitter, and perpendicular, which is reflected from the beamsplitter. The separated beams are then focused with the 1/2" aspheric lenses, which have a focal length of 10 mm, onto the photodetectors.

The photodetectors are indium-gallium-arsenid (InGaAs) avalanche photodiodes (APD) with an active area diameter of 200 µm and a bandwidth of 50 MHz. Compared to Silicon APDs,

InGaAs APDs have a high intrinsic capacitance which leads to a smaller active area for the same bandwidth. In order to compensate for spherical aberrations, aspherical lenses are required to image the received light completely onto the photodiode, thus optimizing the sensitivity.

The specifications of the lidar system are provided in Tab. 1

Table 1. Technical specifications of the polarization lidar system.

Laser	
Mode of operation	Pulsed
Polarization	Linear
Operating wavelength	1550 nm
Pulse duration	8 ns
Pulse repetition frequency	20 kHz
Average power	1000 mW
Energy per pulse	50 µJ
Peak power	6.25 kW
Detector	
Output bandwidth (3 dB)	DC - 50 MHz
Active area diameter	0.2 mm
M factor	10
Minimum NEP (DC - 50 MHz)	$0.46\,\mathrm{pW}/\sqrt{\mathrm{Hz}}$

The electrical signals of the APDs are sent through RF limiters and 50 Ω inline resistors to the data acquisition unit. The function of the limiters is to restrict the electrical signal to a maximum value of 0.8 V, thereby protecting the electronic components from damage. The objective of installing 50 Ω resistors was to achieve impedance matching [13]. As data acquisition unit a RedPitaya STEMlab 125-14-Z7020 low-noise is used, which comprises an analog-to-digital converter (ADC) and a field programmable gate array (FPGA). The signal and data handling in the RedPitaya is illustrated in Fig. 2 and shows the operation of a two channel coherent transient averager. The methodology of coherent averaging is well described in [14].

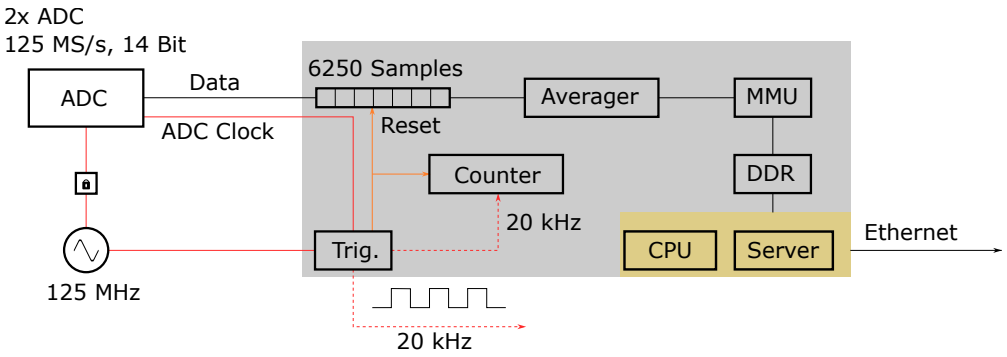

Fig. 2. Schematic illustration of the data acquisition in the FPGA.

The electrical signal from the APDs is converted to a digital signal with the ADCs and proceeded in the FPGA. In the initial phase, the data are transferred to the FPGA, with 6250 values being written to the buffer. Subsequently, the following 6250 values are added to the initial 6250. This process is repeated a specified number of times, which is defined by the user as averaging factor, and the number of repetitions is counted by a counter. Upon completion of the designated number of repetitions, a reset is initiated, whereby the current buffer is sent to the memory management unit (MMU). The counter is reset to zero, the clock is reset, and the process is reinitiated. The essential element of this data acquisition scheme is a shared clock in the FPGA that serves to trigger the laser on one hand and the counter on the other, with a delay corresponding to the latency between the trigger and the output of the laser pulse.

The majority of the utilized components, particularly the lenses, detectors, and lens mounts, are commercial off-the-shelf (COTS) components. Furthermore, a custom-designed 3D-printed baseplate and solar shield were developed to mount the COTS components and to block the sun's rays. The assembled optomechanic is depicted in Fig. 3, in a computer-aided design (CAD) model.

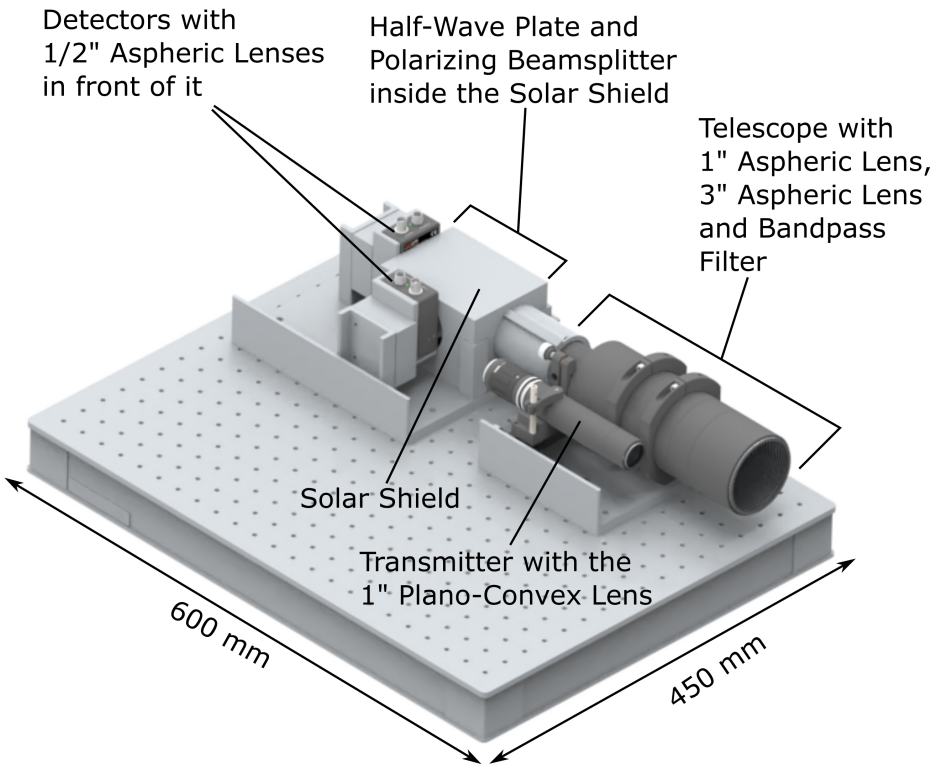

Fig. 3. CAD model of the optomechanical assembly of the polarization lidar fit on a 600 mm × 450 mm breadboard

The size of the optiomechnic system is 525 mm × 195 mm × 95 mm, and the entire system, including laser and RedPitaya fit on a 600 mm × 450 mm breadboard, depict in Fig. 4.

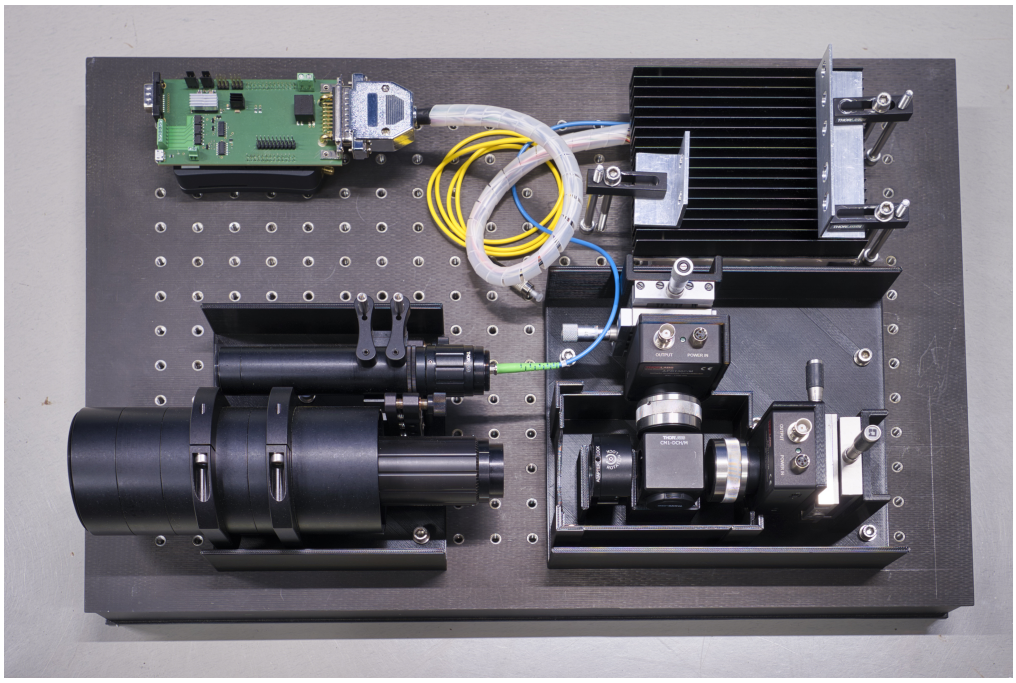

Fig. 4. Photograph of the polarization lidar, including the optomechanics, laser, and RedPitaya fit on a breadboard in the laboratory, with the solar shield removed.

3. Method

3.1. Estimation of the depolarization ratio

In order to calculate the received power signal of the lidar system, the following lidar equation can be used, which is

$$P(R,\lambda) = P_0 \, \frac{c\,\tau}{2} \, A \, \eta \, \frac{O(R)}{R^2} \, \beta(R,\lambda) \, \exp\left[-2 \int_0^R \alpha(r,\lambda) \, \mathrm{d}r\right] \tag{1}$$

with the received power $P(R,\lambda)$, the average power of a single laser pulse P_0, the speed of light c, the pulse length τ, the area of the receiving telescope A, the efficiency factor η, the overlap function $O(R)$, the distance R, the backscatter coefficient β and the extinction coefficient α. [15] P_0, τ and A are system parameters and defined by the system itself and c is a natural constant and thereby also fixed. β and α are unknown and O and η need to be chosen. For the overlap function, the empirical function

$$O(R) = \frac{1}{1 + \exp(-k \, (R - R_0))} \tag{2}$$

is used. The parameter k and R_0 of the overlap function and the efficiency factor are selected in a manner that ensures that the received power curve of the developed polarization lidar aligns with the received power curve of the Deutscher Wetterdienst (DWD) lidar at Schnarrenberg in Stuttgart for each channel. The data were acquired from E-Profile as part of the European Meteorological Network (EUMETNET) [16].

The lack of knowledge regarding the backscatter and extinction coefficients, the lidar equation cannot be solved for the backscatter coefficient, which is typically used to determine the depolarization ratio. A reduction in the number of unknowns in the lidar equation is one method

for resolving this issue [17]. A common approach is to combine the backscatter and extinction coefficients to form the attenuated backscatter coefficient [18]. Consequently, the attenuated backscatter [19]

$$B(R) = \frac{2\ P(R)\ R^2}{P_0\ c\ \tau\ A\ \eta\ O(R)} = \beta(R)\ \exp\left[-2\int_0^R \alpha(r)\mathrm{d}r\right] \tag{3}$$

is used to solve the lidar equation, and the backscatter coefficient is replaced with the attenuated backscatter for calculating the depolarization ratio. The depolarization ratio can thus be written as

$$m = \frac{B(R)_\perp}{B(R)_\parallel}\ G \tag{4}$$

with an additional gain term G to correct differences in the overlap function and the channels efficiency of both channels of the lidar. [17]

3.2. Crosstalk correction

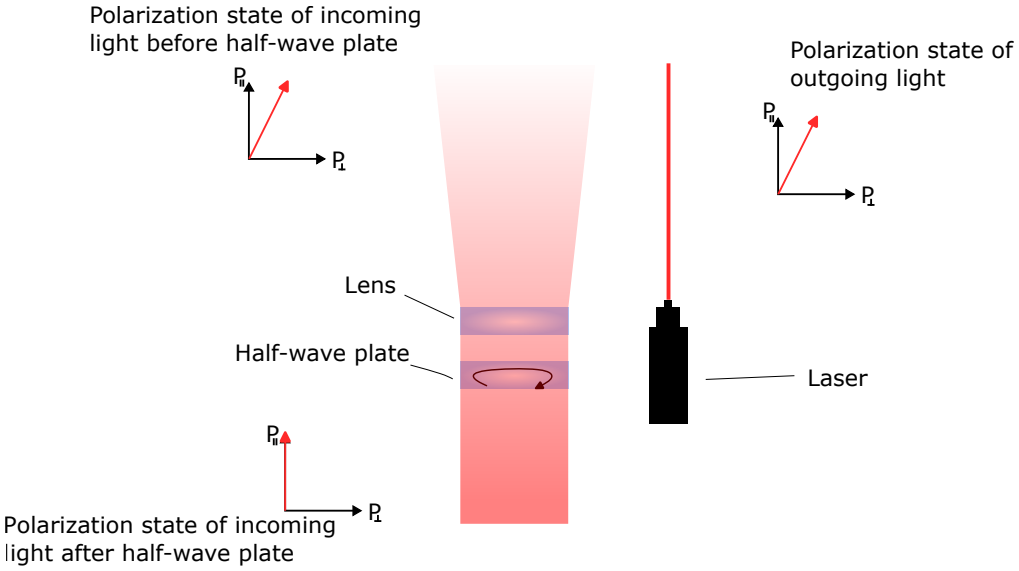

Fig. 5. Illustration of the principle of operation of the half-wave plate for the shift of the polarization plane of the incoming light beam.

As in real lidar systems a phase shift between the transmitter and receiver plane of polarization appears, as illustrated in Fig. 5, a falsification of the depolarization ratio occurs due to crosstalk. To correct most of the crosstalk error, the Δ90 calibration from Freudenthaler [20] was performed. Hence the methodology is well described in [21], this paper presents only the results of the Δ90 calibration. Fig. 6 shows the outcome of the Δ90 calibration with the correction vectors G_{+45}, the G_{-45} and their geometrical mean

$$G_{\Delta 90} = \sqrt{G_{+45}\ G_{-45}}. \tag{5}$$

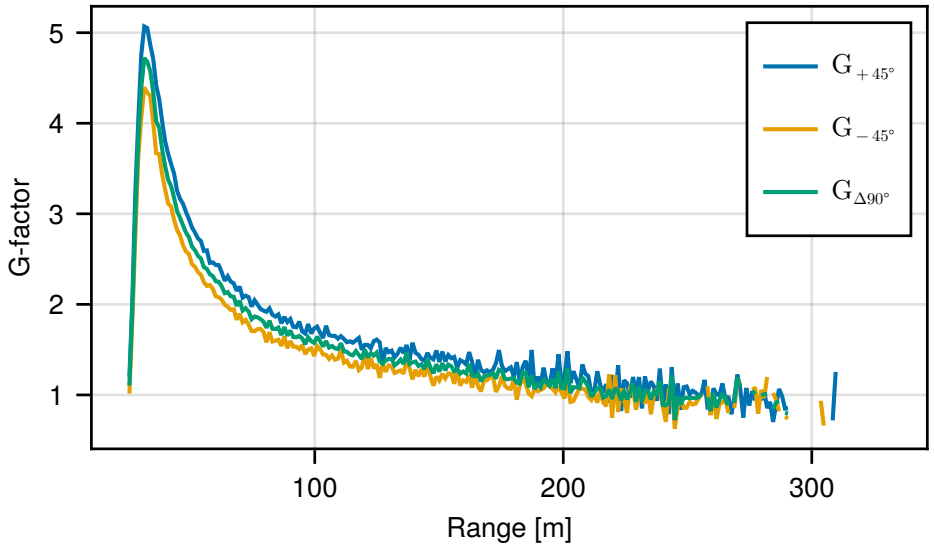

Fig. 6. The estimated G-factor vector for the polarization lidar, resulting from the Δ90 calibration. The integration time of the measurements was 5 min and the optical output power was 1.2 W.

At the beginning the correction factor increases strongly due to the fact of partial overlap of the transmitter and receiver. After approximately 35 m the curve drops and converges towards 1. Most of the differences between the G_{+45} and G_{-45} curves are eliminated trough a good overlap function and channel efficiency. The rest of the differences mostly came from the phase shift of the planes of polarization of the transmitter and receiver and is corrected trough the geometrical mean $G_{\Delta 90}$. The corrected depolarization ratio vector is

$$m_{\text{corrected}} = \frac{m}{G_{\Delta 90}} \tag{6}$$

4. Experimental results

The primary objective of developed polarization lidar is to detect bioaerosols at a certain distance and pre-classify them based on their depolarization ratio. Accordingly, measurements of synthetic aerosols were conducted at the open beam path of the Institute of Technical Physics of the DLR in Lampoldshausen on April 15th, 2024. The open beam path in Lampoldshausen is a 130-meter-long trail that has been specifically designed for laser measurements under atmospheric conditions [22]. The objective was to simulate a possible operational scenario in which the polarization lidar detects bioaerosols at a certain range. Therefore, series of tests were conducted using a variety of aerosol samples. The polarization lidar is positioned at an elevation of 0°. The aerosol sources for the synthetic aerosols, which consisted of water mist, unspecified sand, fog, and Arizona road dust, were positioned at a distance of 100 meters. Furthermore, measurements were conducted at a methane flare present on the site of the open beam path. Accordingly, the polarization lidar was elevated to an angle of 10° for that particular measurement. An average laser output power of 1200 mW was selected. For data processing an integration time of 0.2 s was chosen. A list of the parameters utilized in the experimental setup can be found in Tab. 2. A photographic representation of the experimental environment of the open beam path, situated in

Lampoldshausen, is depicted in Fig. 7.

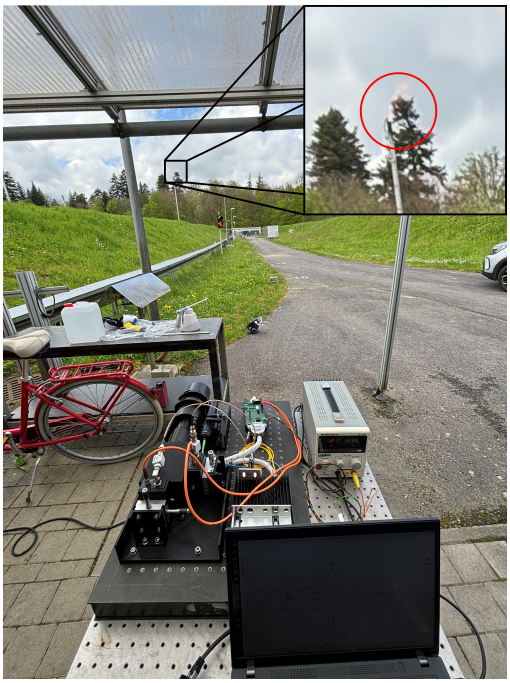

Fig. 7. Photography of the polarization lidar during the open beam path experiments at the DLR in Lampoldshausen. The methane flare is zoomed in and highlighted in red.

Table 2. Experimental parameters for the open beam path experiment at the DLR in Lampoldshausen.

Integration time	0.2 s
Average laser output power	1200 mW
Elevation	0°
Elevation methane flare	10°

In order to investigate the experimental results, two different types of figures were chosen. The initial type of figure is a combination of three heat map plots. The upper heat map depicts the data from the parallel polarized light channel, the middle heat map shows the data from the perpendicular polarized light channel, and the lower heat map illustrates the depolarization ratio. The vertical axis of each heat map plot represents the range in meters, while the horizontal axis denotes time in Coordinated Universal Time (UTC). The color bar of the top and middle heat maps represent the log10 attenuated backscatter, while the color bar of the bottom heat map represents the depolarization ratio.
The second type of figure is a so-called raincloud plot, which is a combination of a histogram, a box plot, and a scatter plot. In the raincloud plot, the depolarization ratio of the following synthetic aerosols is represented: water mist, methane flare, fog, Arizona road dust, and sand.
While experiments were conducted with a variety of aerosols, this paper will focus on the heat maps of the synthetic aerosols sand and fog as illustrative examples of depolarizing and

non-depolarizing aerosols, respectively. A comparison of all the aerosols under investigation is provided in the raincloud plot.

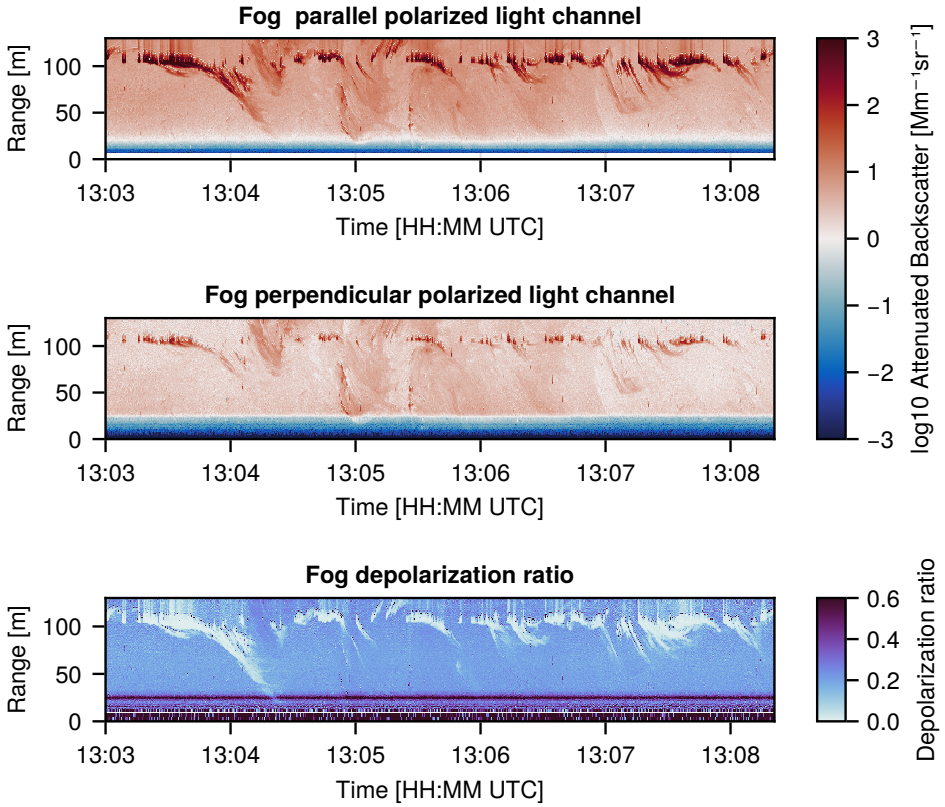

Fig. 8. Heatmaps of the fog experiment. On top the parallel polarized light channel and in the middle the perpendicular polarized light channel as log10 attenuated backscatter. On bottom the depolarization ratio.

One of the experiments conducted was an investigation of fog produced with a fog machine. Therefore, the Stairville fog fluid type E-M was used to produce a significant quantity of synthetic aerosol. This can be observed in the attenuated backscatter heat maps of the parallel and perpendicular polarized light channels, as well as the depolarization ratio, as illustrated in Fig. 8. The synthetic aerosol fog was generated at a distance of approximately 100 m. The fog machine produced a fluid that was dispersed throughout the entire area, thereby illustrating the atmospheric dynamics as the fog is transported by wind. Furthermore, the strong attenuated backscatter from the atmosphere is observable. Given that Lampoldshausen is located in an area surrounded by forest, the presence of pollen results in an increase in the attenuated backscatter of the atmosphere. The most noteworthy aspect is the depolarization ratio, which shows a clear distinction between the atmosphere and the synthetic aerosol fog. The depolarization ratio of the fog is observed to be lower, with a value approaching zero, in comparison to that of the atmosphere, which exhibits an approximate depolarization ratio of 0.2. The attenuated backscatter signal observed in the perpendicular polarized light channel can be attributed to crosstalk.

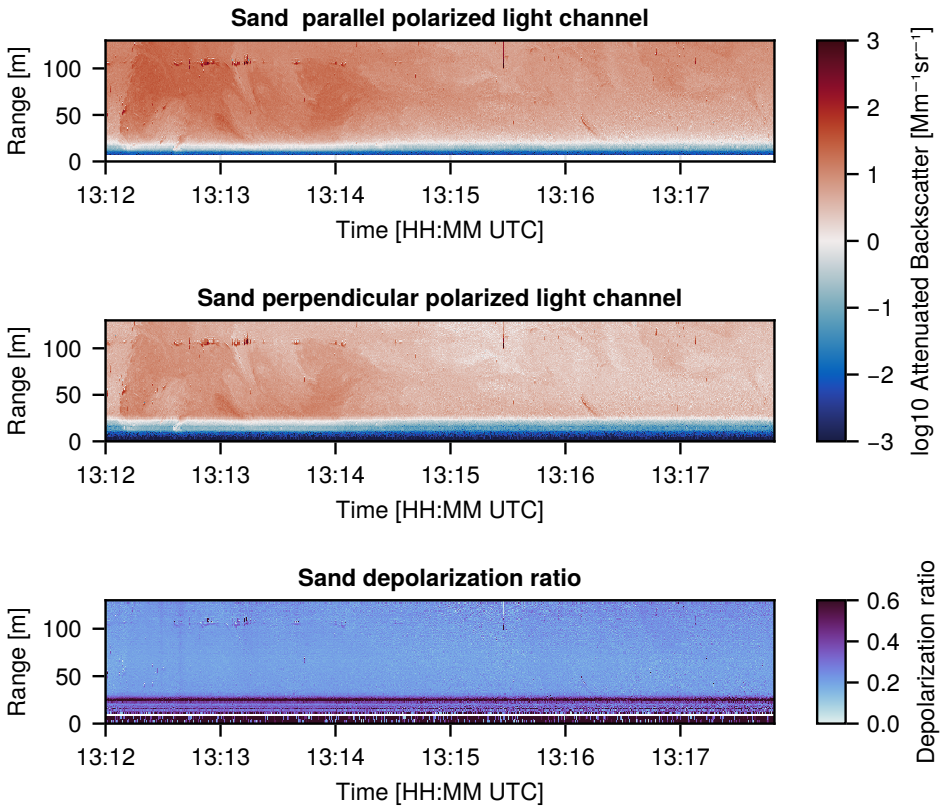

Fig. 9. Heatmaps of the sand experiment. On top the parallel polarized light channel and in the middle the perpendicular polarized light channel as log10 attenuated backscatter. On bottom the depolarization ratio.

A further synthetic aerosol test, conducted using the polarization lidar, was a sand experiment. In contrast to fog, sand is assumed to depolarize the laser light transmitted from the polarization lidar. This phenomenon can be observed in Fig. 9, which depicts the heat maps of the attenuated backscatter of the parallel and perpendicular polarized light channels and the depolarization ratio. Similar to the fog measurement, there is a strong background attenuated backscatter from the atmosphere, which can be seen in the parallel and perpendicular polarized light channels. At about 100 m the sand was sprayed with pressurized nitrogen as a synthetic aerosol. This can be seen in the discontinuous strong backscatter signals at this distance. At 13:15:30 UTC a single event happened where the origin is unknown but from the shape of the signal it looks like a hard target. This may have happened while preparing some sand for the measurements. At approximately 50 m between 13:12:00 UTC and 13:12:30 UTC, sand can be observed that was whirled up on the ground during the experiment and transported by the wind to the entire open beam path. In front of 100 m, especially between 13:12 UTC and 13:14 UTC, there is a moving aerosol with a strong backscatter signal about the entire range of 130 m. These are most likely pollen, which heavily polluted the atmosphere. The pollen can be identified in the depolarization heatmap, as there is no change in depolarization in areas with increasing backscatter signal. The concentration of pollen have increased in some areas during the experimental period due to wind transport. As a consequence of this pollution, the atmospheric dynamics over time

can be observed in the heatmap of the parallel polarized light channel, caused by wind, which creates areas with varying densities of pollution. The movement of the pollen observed between 13:12 UTC and 13:14 UTC demonstrate the well spacial resolution of the polarization lidar with approximately 2.8 m, which allows to resolve the atmospheric dynamics that have driven the pollen over the range and causes different dense layers of pollen. Compared to the fog measurements, in the depolarization ratio heatmap clear differences are observable. While the depolarization ratio of fog is lower than that of the atmosphere, the depolarization ratio of sand is higher than that of the atmosphere. This shows the different polarizing characteristics of these two synthetic aerosols.

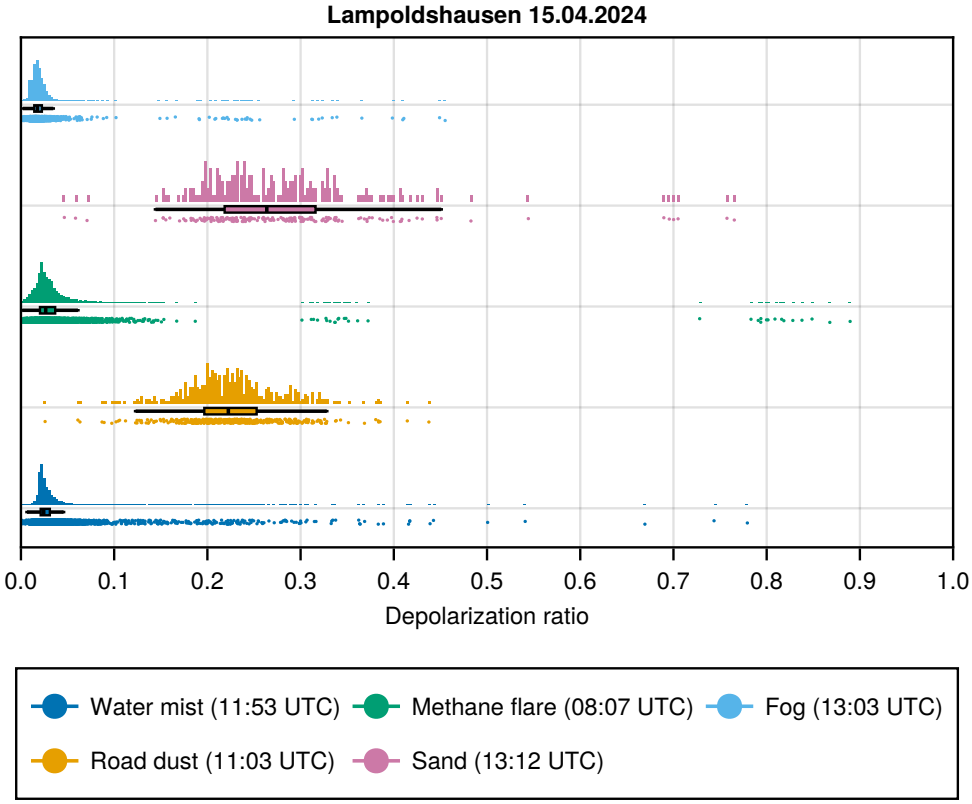

Fig. 10. Distributions of water mist, methane, fog, road dust and sand depolarization ratios during open beam path experiments.

The raincloud plot in Fig. 10 is a comparative analysis of the distributions of depolarization ratios of aerosols on the open beam path at Lampoldshausen. Due to the considerable influence of the atmospheric background, it was necessary to apply a filtering process in order to extract the depolarization ratio from the aerosols. This is achieved by ignoring the weak backscatter signals of the atmosphere and utilising only the strong backscatter signals to determine the depolarization ratio. In this approach, the underlying assumption is that the backscatter of synthetic aerosols is stronger than that of the atmosphere, which is a condition for the polarization lidar to detect synthetic aerosols, as aerosols that scatter weaker than the atmosphere cannot be detected. It is clearly visible that the depolarization ratios of water mist and fog were close to zero. This is due

to the fact that fog and water mist are spherical, homogeneous particles that cause almost no depolarization. It is noteworthy that the depolarization ratio of the methane flare is also nearly zero. This might be due to the fact that methane was burned in a clean combustion process which led to the chemical reaction [23]

$$CH_4 + 2\,O_2 \longrightarrow 2\,H_2O + CO_2 \tag{7}$$

with methane (CH_4), molecular oxygen (O_2), water (H_2O), and carbon dioxide (CO_2) as the reactants and products, respectively. Eq. 7 shows that water is produced as a result of combustion, which possibly condensed on condensation nuclei such as pollen and turned into water droplets. This could explain the depolarization ratio towards zero, because only the water aerosols are measurable, while carbon dioxide remains gaseous and is not detectable by an aerosol lidar. The data clearly indicate that depolarization is present in the measurements of sand and road dust.

Even if the distributions look similar, the distribution of sand is broader than that of road dust. The first quartile of sand is 0.22 and the third quartile is 0.32, while the first quartile of road dust is 0.2 and the third quartile is 0.25. However, the median values are close to each other. The median of sand is 0.26 and the median of road dust is 0.22. The differences in the first and third quartiles can be explained by the fact that sand consists of different grain sizes between 0 mm–2 mm [24], whereas road dust has a well-defined grain size distribution mostly smaller than 100 µm [25]. For this reason, the distribution of road dust is more narrow. As both substances share similar properties as expected from sand-like particles, the median of the distribution of the depolarization ratio is in the same range around 0.25.

The results of the measurements of synthetic aerosols on the open beam path in Lampoldshausen demonstrate the feasibility of detecting synthetic aerosols at a certain distance with the developed polarization lidar. Furthermore, the high spatial resolution allows for precise localization of the aerosols. The high spatial resolution is especially visible in the dynamics of the background atmosphere.

In cases of high atmospheric background attenuated backscatter, hard filtering must be performed to separate the synthetic aerosol. As a consequence, only strong backscatter signals from the aerosols can be used, the others vanish in the background signal of the atmosphere. Filtering is very important, even if some aerosol data will be lost. In cases where the atmosphere is highly depolarizing, close to the depolarization of the synthetic aerosol, filtering is essential to distinguish the depolarization ratio of the aerosol from that of the atmosphere.

The most important result of the experiments is that different aerosols, such as fog and sand produce repeatable measurable depolarization ratios, which makes it possible to distinguish between different aerosols based on the depolarization ratio.

5. Conclusion

In this paper the development of a polarization lidar for measuring synthetic aerosols and distinguish them based on their depolarization ratio is described. It was possible to design a lidar with the dimensions 525 mm × 195 mm × 95 mm of the optomechanical part, excluding the RedPitaya and the laser itself. The complete system, including the laser and the RedPitaya, is designed to fit on a breadboard with dimensions 600 mm × 450 mm. The mass of the system is less than 10 kg. To maximize the components availability, a significant part of the system was constructed using COTS components. This included the optics, optomechanics, detectors and the ADC. Only the baseplates were custom designed. The selected laser for the system has a unconventional wavelength of 1550 nm, which is optimal for eye safety. Regardless of the 1550 nm wavelength, the classification as eye safe was not reached due to the fact that the collimated beam after the expanding optic of 1 ” with an average power of 1 W is not eye-safe until a distance of 190 m. For further development of the system an increase of the transmitter aperture and scanning of the laser beam will reduce the maximum possible exposure time and

result in an eye-safe operation of the system. Since it was possible to detect clouds at a distance of several kilometers with the system, it can be assumed that the system can also detect aerosols at a greater distance than the 100 m used here. The spatial resolution of approximately 2.8 m is achieved by the 8 ns pulse duration of the laser, which theoretically leads to a spatial resolution of 1.4 m. However, due to the inevitable losses incurred through the bandwidth of the detector, a spatial resolution of approximately 2.8 m is achieved. The housing of the system within a solar shield and the use of a bandpass filter have enabled the system to be used in daylight, as all experiments were conducted during daylight hours. During experiments, it was demonstrated that the system is capable of measuring the depolarization of various aerosols and distinguishing them based on their depolarization ratio. Furthermore, it was demonstrated that measurements could be conducted at a distance of 100 m. While this range is not particularly long for an atmospheric lidar, it should be stressed out, that this work focuses on the technical aspects of the depolarization lidar technique. Especially eye-safe IR wavelengths, small system size, embedded data processing and potential for mobile low-power daylight applications. Additionally, the system is capable of distinguishing between a strong atmospheric background and synthetic aerosols due to effective filtering. Moreover, it was demonstrated that the transport of synthetic aerosols in different distances over time can be observed, thereby confirming the high spatial resolution. The presented systems size, weight and power requirements can be further reduced. This allows to use the depolarization technique as a safe, compact and mobile scanning technique for ground-based detection of unknown aerosol sources.

Acknowledgments

I would like to thank Christoph Geiß for organizing the measurement campaigns in Lampoldshausen and for his support during the measurement campaigns.
I would also like to thank Samantha Siegert for proofreading this paper.

Disclosures

The authors declare that there are no conflicts of interest related to this article.

Data Availability Statement

Data underlying the results presented in this paper are not publicly available at this time but may be obtained from the authors upon reasonable request.

References

1. J. H. Seinfeld and S. N. Pandis, *Atmospheric Chemistry and Physics: From Air Pollution to Climate Change* (John Wiley & Sons, 2016).
2. U. Pöschl, "Atmospheric aerosols: composition, transformation, climate and health effects," Angewandte Chemie Int. Ed. **44**, 7520–7540 (2005).
3. W. H. Organization, "Who global air quality guidelines: particulate matter (pm2.5 and pm10), ozone, nitrogen dioxide, sulfur dioxide and carbon monoxide," https://www.who.int/publications/i/item/9789240034228 (2021).
4. W. C. Hinds, *Aerosol Technology: Properties, Behavior, and Measurement of Airborne Particles* (John Wiley & Sons, 1999).
5. M. O. Andreae and D. Rosenfeld, "Aerosol–cloud–precipitation interactions," Earth-Science Rev. **89**, 13–41 (2008).
6. V. R. Després, J. A. Huffman, S. M. Burrows *et al.*, "Primary biological aerosol particles in the atmosphere: a review," Tellus B: Chem. Phys. Meteorol. **64**, 15598 (2012).
7. M. I. Mishchenko, L. D. Travis, and A. A. Lacis, *Scattering, Absorption, and Emission of Light by Small Particles* (Cambridge University Press, 2002).
8. M. Kampa and E. Castanas, "Human health effects of air pollution," Environ. Pollut. **151**, 362–367 (2008).
9. M. Grella, J. Maffia, E. Dinuccio, *et al.*, "Assessment of fine droplets (<10 µm) in primary airborne spray drift: A new methodological approach," J. Aerosol Sci. **169**, 106138 (2023).
10. A. Tsekeri, V. Amiridis, A. Louridas, *et al.*, "Polarization lidar for detecting dust orientation: system design and calibration," Atmospheric Meas. Tech. **14**, 7453–7474 (2021).

11. R. Yu, Q. Wang, G. Dai, *et al.*, "The design and performance evaluation of a 1550 nm all-fiber dual-polarization coherent doppler lidar for atmospheric aerosol measurements," Remote. Sens. **15** (2023).
12. J. Harms, "Lidar return signals for coaxial and noncoaxial systems with central obstruction," Appl. Opt. **18**, 1559–1566 (1979).
13. J. Langner, "Hochfrequenz-verstärker," in *Elektronik für Ingenieure und Naturwissenschaftler,* (Springer Berlin Heidelberg, Berlin, Heidelberg, 2014), pp. 255–278.
14. R. G. Lyons, *Understanding Digital Signal Processing* (Prentice Hall, 2004).
15. U. Wandinger, "Introduction to Lidar," in *Lidar: Range-Resolved Optical Remote Sensing of the Atmosphere,* C. Weitkamp, ed. (Springer New York, New York, NY, 2005), pp. 1–18.
16. "E-Profile Eumetnet," https://e-profile.eu/cm_profile?measurement_date_str=2024-11-22&cm_instrument_type=&ql_size=80&ql_show=true&zoom_level=6 (2024).
17. C. Ritter and C. Münkel, "Backscatter Lidar for Aerosol and Cloud Profiling," in *Springer Handbook of Atmospheric Measurements,* T. Foken, ed. (Springer International Publishing, Cham, 2021), pp. 683–717.
18. R. R. Rogers, C. A. Hostetler, J. W. Hair, *et al.*, "Assessment of the CALIPSO Lidar 532 nm attenuated backscatter calibration using the NASA LaRC airborne High Spectral Resolution Lidar," Atmospheric Chem. Phys. **11**, 1295–1311 (2011).
19. F. Szczap, A. Alkasem, V. Shcherbakov, *et al.*, "Computation of the Attenuated Backscattering Coefficient by the Backscattering Lidar Signal Simulator (BLISS) in the Framework of the CALIOP/CALIPSO Observations," Atmosphere **14** (2023).
20. V. Freudenthaler, M. Esselborn, M. Wiegner, *et al.*, "Depolarization ratio profiling at several wavelengths in pure saharan dust during samum 2006," Tellus B: Chem. Phys. Meteorol. (2009).
21. V. Freudenthaler, "About the effects of polarising optics on lidar signals and the Δ90 calibration," Atmos. Meas. Tech. **9**, 4181–4255 (2016).
22. "Laserlabor mit Freistrahlstrecke," https://www.dlr.de/de/forschung-und-transfer/forschungsinfrastruktur/grossforschungsanlagen/laserlabor-mit-freistrahlstrecke (2024). Accessed: 2024-05-03.
23. B. Sieve, S. Struckmeier, and D. Böhm, "Organische chemie i – kohlenwasserstoffe," in *Experimente im Chemieunterricht Band 2 : didaktisch begründet auswählen und sicher durchführen,* (Springer Berlin Heidelberg, Berlin, Heidelberg, 2024), pp. 277–338.
24. "Spielsand Sahara," https://weco-naturstein.de/sortiment/spielsand/spielsand-sahara/ (2024). Accessed: 2024-05-07.
25. "PTI Arizona Prüfstaub A2 fine ISO 12103-1," https://testdust.dmt-group.com/normstaeube/pti-arizona-pruefstaub-a2-fine (2024). Accessed: 2024-05-05.